Slow coarsening in unstable liquid films under gravity on a disordered substrate

Avanish Kumar,[1] Chaitanya Narayanam,[2] Rajesh Khanna,[2] and Sanjay Puri[1]
[1]*School of Physical Sciences, Jawaharlal Nehru University, New Delhi 110067, India*
[2]*Department of Chemical Engineering, Indian Institute of Technology Delhi, New Delhi 110016, India*

(Received 6 September 2019; accepted 11 March 2020; published 2 April 2020)

We study the evolution of unstable liquid films via numerical solutions of the thin-film equation. The film is placed on a coated substrate with disorder. This is modeled by a random spatial variation of the relative value of the Hamaker constants for the substrate and coating. The free energy consists of (a) the van der Waals term for the substrate/coating interactions with the film and (b) a term due to gravity. This free energy admits a Maxwell double-tangent construction with two coexisting phases, i.e., "thin" and "thick" phases. In the absence of disorder, the film dewets by true morphological phase separation (MPS), i.e., the elimination of domain walls between the coexisting phases. The introduction of disorder may result in the trapping of these domain walls, with a drastic slowdown in growth kinetics. We present detailed numerical results in $D = 2$ and $D = 3$ to understand this slow coarsening, where D is the dimensionality of the liquid-film system.

DOI: 10.1103/PhysRevE.101.042801

I. INTRODUCTION

A homogeneous thin film on a substrate may be spontaneously unstable to segregation into thin and thick regions, depending on the film thickness [1–10]. We stress that the liquid film does not undergo phase change during this evolution; i.e., it stays in the liquid phase. A free-energy functional which admits a double-tangent construction characterizes the film under the influence of gravity. This segregation has been termed "true morphological phase separation" (true MPS) [11,12], owing to the formation of two true equilibrium phases (thin and thick), unlike dewetting in thin films not influenced by gravity [13]. In the latter case, dewetting proceeds via MPS, where the film phase separates into an equilibrium thin phase and a defect phase whose height diverges to infinity. The thin and thick phases in true MPS correspond to the two equilibrium liquid-film heights which are obtained by the Maxwell double-tangent construction on the free energy of the liquid-film system (which will be presented shortly). Therefore, "thin" and "thick" denote the minimum and maximum heights which the liquid film can attain during self-organization.

Two distinct pathways of true MPS have been observed, namely the "defect pathway" and the "direct pathway":

(a) The evolution of an unstable film closer to the thin phase results in the appearance of an equilibrium flat film and circular droplets [11,12]. The flat film corresponds to the thin phase. The droplets have a range of thicknesses and are termed defects. These defects are not at local equilibrium. Thus, coarsening proceeds at a rapid pace until the droplets reach the thickness corresponding to the thick phase. Clearly, there may be a considerable delay in the appearance of the thicker phase. This pathway has been termed as the defect pathway [11,12]. The free-energy functional for these thin-film systems is often asymmetric, and most of the unstable film thicknesses are closer to the thin phase. Therefore, most of the films undergoing true MPS follow the defect pathway. The duration of the defect-coarsening stage depends on the initial thickness of the film.

For films that are closer to the thick phase, the thick phase appears first in a "reverse defect pathway." The evolution is characterized by a pattern with a percolating thick phase with circular holes.

(b) Films with initial thickness midway between the equilibrium phases undergo true MPS through the direct pathway. Here, both the thin and thick phases appear at approximately the same time. The coexisting phases coarsen via an evaporation-condensation mechanism. A bicontinuous morphology is observed for thin films undergoing true MPS through the direct pathway.

Disorder, either physical or chemical, is a standard feature of self-organizing systems. The presence of disorder which is mobile (annealed) or immobile (quenched) can hinder pattern formation in some cases [14]. However, in other cases, disorder may provide a template for the formation of unique patterns [15,16]. An understanding of the effects of random disorder is essential for experimentalists, because real-life substrates are neither smooth nor homogeneous. Many experiments on relatively homogeneous substrates show departure from the usual pathways for MPS [17]. These observations suggest the presence of heterogeneous sites, e.g., dust particles, microcavities, chemical contamination, variation of oxide layer thickness on silicon, variable chain adsorption, etc. This results in the formation of localized patches with surface properties different from those of the surrounding substrate [18].

For coated substrates, the chances of random disorder being present on the substrate are higher due to the possibility of uneven coating or impurities in the coating material. Thus, it is important to study the effects of random disorder on a dewetting film.

In earlier work [19], we found the surprising result that quenched disorder only affects the early stages of MPS—the late stages of MPS are not affected by disorder. This is because

disorder sites are unable to effectively trap the continuously steepening defect boundaries. This result is experimentally important because it shows that the universal aspects of MPS kinetics are independent of disorder. In this paper, we turn our attention to the effects of quenched disorder on the kinetics of *true MPS*. The primary narrative of this paper is as follows. We have seen that the incorporation of gravity terms in the free energy of a thin film enables existence of two genuine equilibrium phases (thin and thick). In this case, dewetting proceeds via the formation and motion of interfaces between the thin and thick phases, a process which we term as "true MPS." This process is analogous to the more extensively studied problem of spinodal phase separation (SPS) in binary mixtures [1,11]. Using insights gained from SPS [20–23], we expect true MPS to be drastically slowed down by interface trapping at sites of quenched disorder. This paper shows that the real situation is considerably more subtle due to the highly asymmetric free energy in the present problem. For true MPS through the direct pathway, the system establishes interfaces between equilibrium phases at early times. These are indeed trapped by disorder, yielding logarithmic coarsening analogous to that in SPS [23]. However, for true MPS through the defect pathway, there is no formation of equilibrium interfaces for prolonged time windows, as the film does not have enough time to saturate to its thick phase. This situation is analogous to MPS; i.e., the disorder is irrelevant as it cannot trap the ever-steepening interfaces. Thus, one sees an extended regime of power-law growth similar to that in the disorder-free system. An experimentalist can access both the direct and defect pathways of true MPS by tuning the initial film thickness vis-à-vis the free energy. Thus, the above predictions can be tested experimentally.

This paper is organized as follows. In Sec. II, we discuss a mathematical model of the substrate-film system with random disorder. We also provide details of our simulation. In Sec. III, we present detailed results for the kinetics of true MPS with disorder. We will study growth laws and other statistical measures characterizing the evolving patterns. In Sec. III A, we discuss morphological evolution in $D = 2$ liquid films with random disorder. In Sec. III B, we describe the effects of random disorder in $D = 3$ liquid films. Here, D is the dimensionality of the liquid-film system. Thus, $D = 2$ corresponds to a one-dimensional substrate, with the film height along the perpendicular axis. Similarly, $D = 3$ corresponds to a two-dimensional substrate. Clearly, $d = D - 1$ is the dimensionality of the substrate. Finally, in Sec. IV, we conclude this paper with a summary and discussion of our results.

II. THIN-FILM MODEL AND SIMULATION DETAILS

The standard thin-film evolution equation is derived by the application of the lubrication approximation [3] to hydrodynamic equations of motion. (The relevant derivation is provided in the Appendix.) In the lubrication approximation, the lateral size of the liquid film is much larger than its height. Let L and h be the sizes of the film in the lateral and vertical directions, respectively. When the Navier-Stokes equation is written in terms of h/L, we obtain different terms involving powers of h/L. In the lubrication approximation, we focus on the limit $h/L \ll 1$. We also consider very low Reynolds number, which is the ratio of the inertial and viscous shear forces, i.e., the inertia is negligible compared to the viscosity, and fluid flow is Stokes flow.

The thin-film equation has been used extensively for studies of dewetting and MPS in liquid films [1]. It can be written [13] in a form similar to the Cahn-Hilliard (CH) equation [24,25] of phase-separation kinetics:

$$\frac{\partial}{\partial t}H(\vec{X},t) = \vec{\nabla}\cdot\left[M\vec{\nabla}\left(\frac{\delta F}{\delta H}\right)\right]. \tag{1}$$

The CH equation models phase separation by the "evaporation-condensation" mechanism, which operates as follows. We emphasize that the term "evaporation" used above should not be confused with the evaporation of the liquid film. Recall that we are only considering situations where the liquid remains liquid. The chemical potential on the surface of a smaller droplet of phase 1 (say, the thick phase) is higher than that on a larger droplet due to the difference in curvature. Thus, smaller droplets of phase 1 shrink, and the surplus material is transported through regions rich in the other phase, say 2 (the thin phase). This material then settles elsewhere on larger droplets of phase 1. A similar scenario applies to droplets of phase 2.

The above dynamical equation is written in dimensionless units, and we will set the length scales and timescales below. In Eq. (1), $H(\vec{X},t)$ is the height of the film at space-point $\vec{X}$ (lying on the substrate) and time t. We will refer to a film on a substrate of dimensionality d as a D-dimensional system, where $D = d + 1$. We study cases with $D = 2, 3$ or $d = 1, 2$. The mobility is height dependent with $M(H) = H^3$, corresponding to the no-slip condition of the Stokes flow (see Appendix). The free-energy functional in Eq. (1) is given by

$$F\{H\} = \int d\vec{r}\left[f(H) + \frac{1}{2}(\vec{\nabla}H)^2\right], \tag{2}$$

where $f(H)$ is the local free-energy density and the square-gradient term represents the interfacial tension.

To set length scales and timescales, let us consider the dimensional form of the local free energy $e(h)$, where $h(\vec{r},\tau)$ is the dimensional height field at time τ. Consider a liquid film on a substrate with a coating of thickness d. The substrate provides a long-range Lifshitz–van der Waals attraction, and the coating provides a relatively short-range Lifshitz–van der Waals repulsion [1,11,12]:

$$e(h) = \frac{A_c d_0^2}{h^2} + \frac{(A_s - A_c)d_0^2}{(h+d)^2} + \frac{1}{2}\rho g h^2. \tag{3}$$

Here, $A_c > 0$ is the spreading coefficient of liquid on the coating in the presence of a bounding fluid, and $A_s < 0$ is the spreading coefficient of liquid on the substrate. The quantity d_0 is the closest distance of approach of the film and is nonzero to prevent unphysical divergence of the force field as $h \to 0$. The liquid density is ρ, and g is the acceleration due to gravity.

The chemical potential [$\phi = e'(h)$] and the spinodal parameter [$e''(h)$] are

$$e'(h) = -2A_s\frac{d_0^2}{h^3}\left[\frac{1-B}{(1+d/h)^3}+B\right]+\rho g h, \quad B=\frac{A_c}{A_s},$$
$$e''(h) = 6A_s\frac{d_0^2}{h^4}\left[\frac{1-B}{(1+d/h)^4}+B\right]+\rho g. \tag{4}$$

The characteristic length and timescales are [1]

$$\xi = \frac{h_0^2}{d_0}\left(\frac{\gamma}{6|A_s|}\right)^{1/2},$$
$$\tau_0 = \frac{h_0^5}{d_0^4}\frac{\eta\gamma}{12}\left(\frac{1}{A_s}\right)^2, \tag{5}$$

where h_0 is the thickness of the homogeneous film. Here, η is the viscosity of the liquid film, and γ is the interfacial tension between the film and the bounding fluid. We also introduce the conjoining pressure:

$$\phi_0 = 6\,\frac{h_0^2}{d_0^2}\,|A_s|. \tag{6}$$

The dimensionless variables used in Eq. (1) are then defined as

$$\vec{X} = \frac{\vec{r}}{\xi}, \quad H = \frac{h}{h_0}, \quad t = \frac{\tau}{\tau_0}. \tag{7}$$

As stated earlier, the thin film is supported on an apolar solid substrate with a nanocoating of wettability $B = A_c/A_s < 0$, where A_c and A_s are also known as Hamaker constants [26] for the coating and substrate, respectively. Then, the dimensionless free-energy density is obtained from Eq. (3) as

$$f(H) = \frac{e(h)}{\phi_0} = -\frac{1}{6}\left[\frac{1-B}{(H+\Delta)^2}+\frac{B}{H^2}-GH^2\right]. \tag{8}$$

In Eq. (8), $\Delta = d/h_0$ is the dimensionless thickness of the coating. Further, $G = \rho g h_0^4/(3d_0^2|A_s|)$ is the strength of gravity.

The functional derivative of the free energy in Eq. (2) yields

$$\frac{\delta F}{\delta H} = f'(H) - \nabla^2 H. \tag{9}$$

We substitute Eqs. (8) and (9) in Eq. (1) to obtain the following nonlinear model for the evolution of the coated-apolar-gravity system:

$$\frac{\partial H}{\partial t} = \vec{\nabla}\cdot\left\{H^3\vec{\nabla}\left[\frac{1}{3}\left(\frac{1-B}{(H+\Delta)^3}+\frac{B}{H^3}+GH\right)-\nabla^2 H\right]\right\}. \tag{10}$$

The linear stability analysis of Eq. (10) about the initial height $H = 1$ (in dimensionless units) shows that the wavelength corresponding to the most unstable mode is

$$L_M = 4\pi\left[\frac{1+|B|}{(1+\Delta)^4}-|B|-\frac{G}{3}\right]^{-1/2}. \tag{11}$$

The growth of the unstable modes, followed by their nonlinear saturation, results in the formation of two true equilibrium phases, i.e., thin and thick. Their heights are determined by Maxwell's double-tangent construction for $f(H)$, which will be presented shortly.

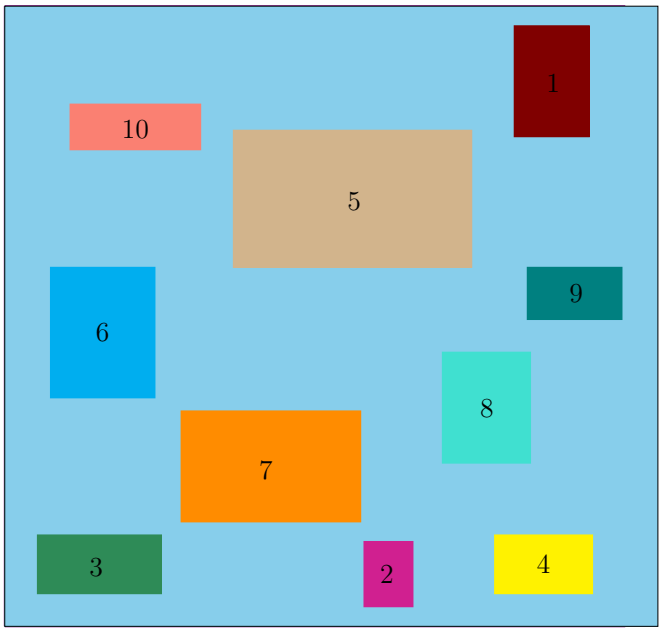

FIG. 1. Schematic diagram of the chemically heterogeneous substrate, i.e., a substrate coated with patches of wettability B_i, $i = 1, 2, 3, \ldots$. The distribution of wettability is random, and the patches are rectangular with random sizes. Each value of B_i corresponds to an asymmetric double-well potential with two finite equilibrium phases H_1 and H_2 (see Fig. 2).

The quenched disorder is introduced through random patches of linear size l and wettability B (see Fig. 1). The mean values of l and B are l_m and B_m. These parameters are uniformly distributed in the intervals $[l_m - \delta l,\ l_m + \delta l]$ and $[B_m - \delta B,\ B_m + \delta B]$, with

$$\frac{\delta l}{l_m} = l_d, \quad \frac{\delta B}{|B_m|} = B_d. \tag{12}$$

In Fig. 2, we show typical free-energy plots [$f(H)$ versus H] for $\Delta = 0.74, 0.32$ and different values of B with $B_m = -0.1$ and $\delta B = 0.025$. The points of double tangency determine the thicknesses of the coexisting phases and are marked on the free-energy plots. Thus, the substrate is segmented into patches with nonuniform sizes and wettability constants. This random disorder is expected to better mimic the experimental situation than striped, checkerboard, or other patterned heterogeneities.

The thin film evolution equation (10) is solved numerically in $D = 2$ and $D = 3$. The initial condition for the simulation consists of small-amplitude random fluctuations ϵ, uniformly distributed in $(-0.01, 0.01)$, about the homogeneous state, namely $H(\vec{X}, 0) = 1 + \epsilon$. The small-amplitude fluctuations in the initial condition mimic thermal fluctuations and are commonly used in the study of domain growth problems [1]. These are required as the homogeneous state $H(\vec{X}, 0) = 1$ is an equilibrium state, though it is unstable. The fluctuations in our initial conditions are two orders of magnitude smaller than the average film height and do not affect the lubrication approximation used in the derivation of the thin-film equation

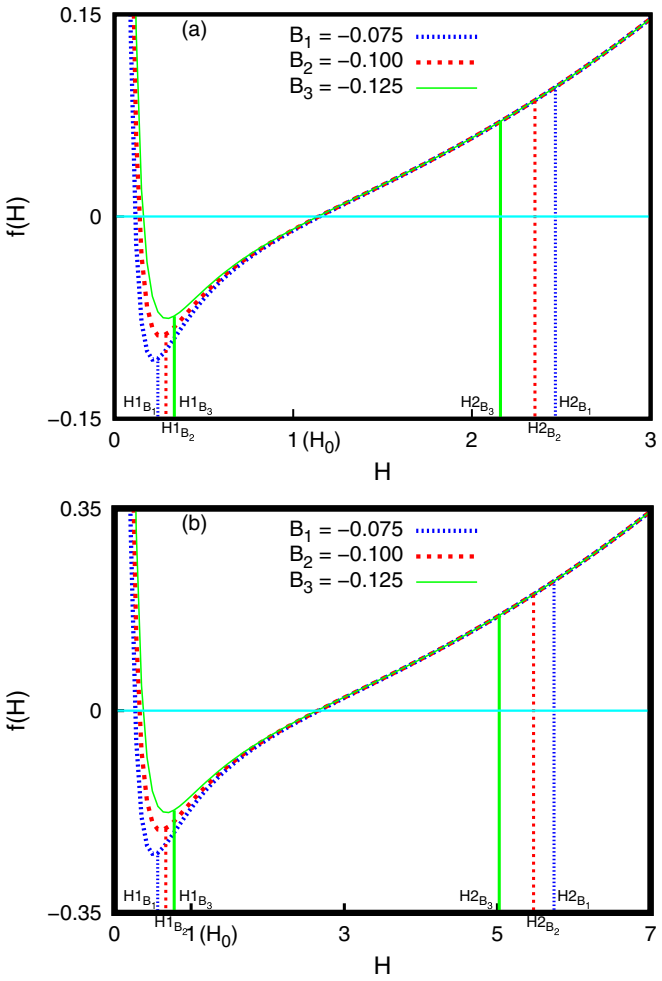

FIG. 2. Dimensionless free energy [$f(H)$ vs H from Eq. (3)] for three different values of wettability B_i. (a) In dimensional units, coating thickness $d = 128$ nm and initial film thickness $h_0 = 400$ nm, so $\Delta = d/h_0 = 0.32$. The strength of gravity is $G = 0.105$. (b) $d = 128$ nm and $h_0 = 172$ nm, so $\Delta = 0.74$. Further, $G = 3.5 \times 10^{-3}$.

(see the Appendix). The system size in $D = 2$ simulations is nL_M, where L_M is the dominant wavelength for $B = B_m$ (n ranges from 16 to 8192). The system size in $D = 3$ simulations is $(16L_M)^2$. Periodic boundary conditions are applied in all directions. A 512-point grid per L_M was found to be sufficient for our numerical study when central differencing in space (with half-node interpolation) was combined with *Gear's algorithm* for time marching. This algorithm is convenient for stiff equations like Eq. (10). The parameters Δ, B_m, and δB were chosen so that the film is always spinodally unstable at $H = 1$. The mean patch size l_m was taken as fL_M, where f varied from $1/16$ to 16. Thus, the size of the patches varied from being much smaller than the spinodal length scale to being much larger than it.

III. DETAILED NUMERICAL RESULTS FOR TRUE MPS WITH DISORDER

We present results from simulations in both $D = 2$ and $D = 3$ to obtain a better understanding of the effects of random disorder on true MPS. The $D = 3$ results provide a realistic scenario for pattern formation in experiments. However, $D = 2$ results enable us to better understand the kinetics, since these simulations can be carried out for very large systems and long times. We remark that the effect of disorder is more pronounced in $D = 2$ simulations. As the transport of liquid is restricted to one direction, the domains may be completely arrested by disorder. On the other hand, coarsening may continue in $D = 3$ as diffusion can take place in multiple directions. Thus, if the droplets can escape the pinning effect of quenched disorder in $D = 2$ systems, they are also able to escape in the corresponding $D = 3$ systems.

A. Case with $D = 2$

We first consider the case with $D = 2$. We will study films of thickness 400 and 172 nm, placed on a substrate with coating of thickness $d = 128$ nm. Thus, the values of $\Delta = d/h_0$ are 0.32 and 0.74, respectively. The patches on the substrate are assigned random values of B. For $B_m = -0.1$ and $\delta B = 0.025$, the free-energy curves of every possible patch are characterized by $B \in [-0.125, -0.075]$. For $\Delta = 0.32$, the free-energy curves are shown in Fig. 2(a). Figure 2(b) corresponds to $\Delta = 0.74$.

Figures 3 and 4 show the evolution of thin films undergoing true MPS on a disordered substrate through the direct and defect pathways, respectively. The disorder profile is shown at the bottom of the snapshots in Figs. 3 and 4. The 400-nm film in Fig. 3 is close to the midpoint of the equilibrium phases—see Fig. 2(a). Thus, the thinner and thicker phases appear simultaneously from the amplification of initial random perturbations. Further, the values of equilibrium phase thicknesses change with the value of B [see Fig. 2(a)]. Since each patch is assigned a random value of B, the domains residing on them will have different equilibrium thicknesses. In Fig. 3, the coarsening of domains freezes during the late stages. The equilibrium domains are pinned to their respective patches. In this case, true MPS is analogous to conventional SPS [1], where the domains are arrested at the sites of disorder [20–23].

The 172-nm liquid film in Fig. 4 lies closer to the thin phase than the thick phase—see Fig. 2(b). Hence, the thick phase appears only after significant coarsening of the droplets (defects) that emerge in conjunction with the flat-film phase from the amplification of initial fluctuations. The bottom panel of Fig. 4 shows that coarsening of the droplets continues unhindered by disorder until they reach the equilibrium thickness. The droplets overcome the pinning effects of the disorder and self-organize until they reach the height of the thick phase. The pinning due to disorder only manifests when the system forms domain walls between two coexisting phases. It can be seen from Fig. 4 that only a few droplets reach equilibrium thickness in the defect pathway.

The kinetics of MPS can be efficiently characterized by studying the time variation of the number of local maxima in the height profile N_m. We exclude bumps (or local maxima) in the flat-film domains by defining an appropriate cutoff for the height variable. This quantity is the inverse of the domain scale, $N_m \sim L(t)^{-1}$.

The top panel of Fig. 5 shows N_m versus t for the true MPS of a 400-nm film on a disordered substrate (cf. Fig. 3) and a

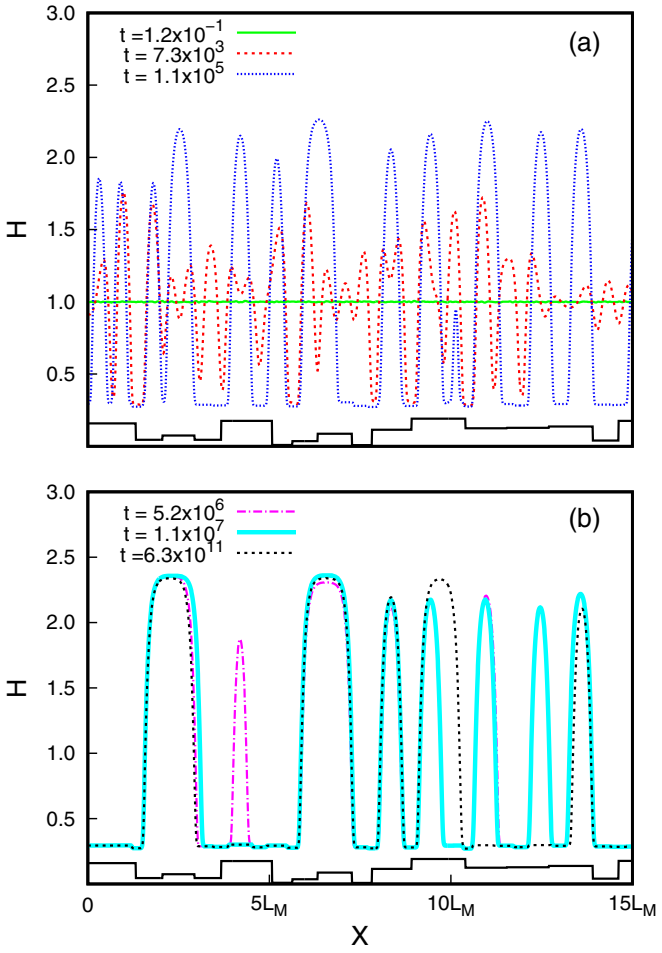

FIG. 3. True MPS of a 400-nm thin film on a 128-nm coating in $D = 2$ through the direct pathway [see Fig. 2(a)]. The top and bottom panels show the nondimensional thickness (H vs X) at the specified nondimensional times. The system size is $8192L_M$, and the simulation parameters are $B_m = -0.1$, $\delta B = 0.05$, $l_m = 256$, and $\delta l = 10$. The strength of gravity is $G = 0.105$.

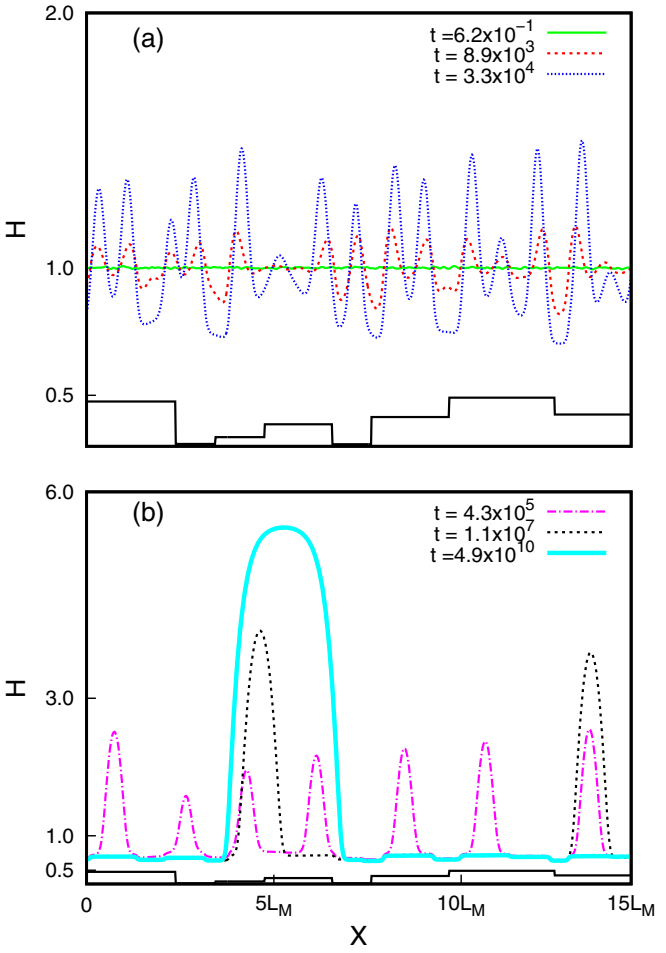

FIG. 4. True MPS of a 172-nm thin film on a 128-nm coating in $D = 2$ through the defect pathway [see Fig. 2(b)]. The top and bottom panels show the nondimensional thickness (H vs X) at the specified nondimensional times. The system size is $8192L_M$, and the simulation parameters are $B_m = -0.1$, $\delta B = 0.05$, $l_m = 256$, and $\delta l = 10$. The strength of gravity is $G = 3.5 \times 10^{-3}$.

homogeneous substrate. The early-stage kinetics of true MPS is similar to that of MPS and is not affected by disorder. This is apparent from the early-time behavior in Fig. 5(a). However, N_m becomes constant in the late stages of true MPS with disorder. The kinetics of true MPS in the 400-nm film without disorder is also slow and is characterized by a logarithmic decay. For the analogous problem of SPS on a line, it is known that late-stage domain growth proceeds logarithmically, i.e., $L(t) \sim \ln(t/t_0)$. This is because the domain walls only interact via their exponentially decaying tails [27]. For the disordered thin-film system studied here, the domains are clearly arrested at the disorder sites. The system can only overcome these disorder barriers via thermal fluctuations, which would appear as noise in our thin-film equation. In this paper, we focus on the deterministic model in Eq. (10).

Figure 5(b) plots N_m versus t for the true MPS of a 172-nm film on a disordered substrate (cf. Fig. 4) and a homogeneous substrate. Recall that this film undergoes true MPS via the defect pathway. It is clear from Fig. 5(b) that the kinetics for both systems is comparable on the timescales of our simulations. In earlier work [13], we have demonstrated that defect-driven coarsening obeys the Lifshitz-Slyozov (LS) growth law: $N_m \sim t^{-1/3}$ or $L \sim t^{1/3}$. We expect disorder effects to show up only when both equilibrium phases are formed and they are separated by genuine domain walls.

In Fig. 6, we show N_m versus t for the true MPS of a 400-nm film on substrates with various disorder strengths [see Fig. 6(a)] and patch sizes [see Fig. 6(b)]. The change in kinetics is comparatively small to variation of the disorder strength. However, it is clear that domains get arrested at smaller length scales for larger disorder amplitude [Fig. 6(a)]. The effect of patch sizes is more significant [see Fig. 6(b)]. The arrest occurs earlier for smaller patch sizes. Further, the coarsening is arrested at smaller length scales for smaller patch sizes.

For self-organizing processes like true MPS, the driving force is the minimization of free energy of the system. The free energy F in Eq. (2) is the sum of the *excess free energy* F_e and the *interfacial free energy* F_i. Figure 7 shows F versus t for the 400-nm film (top panel) and the 172-nm film (bottom

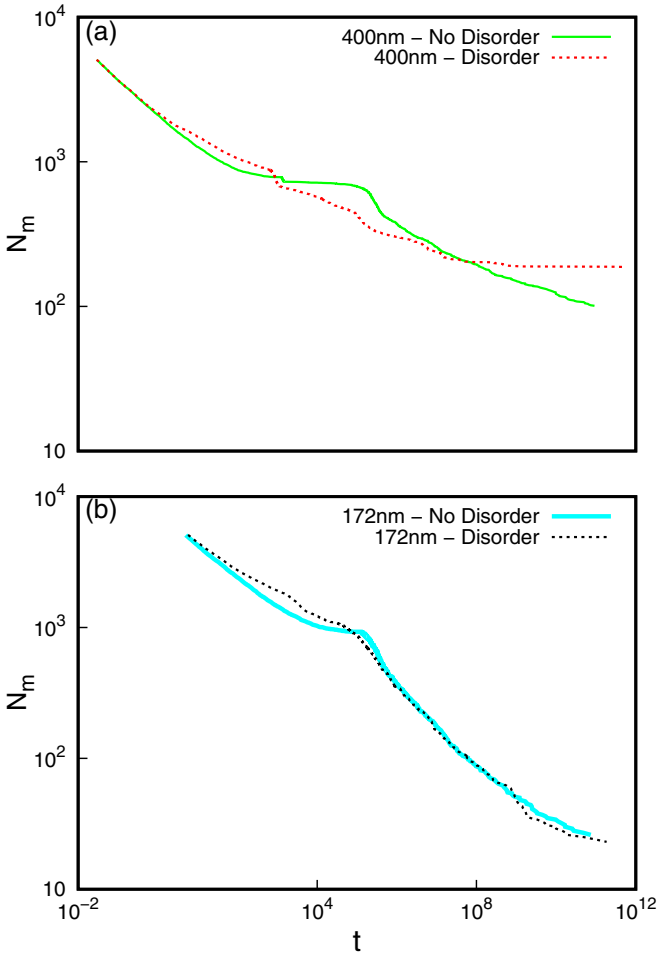

FIG. 5. Variation of number density of local maxima for the 400-nm film in Fig. 3 (top panel) and the 172-nm film in Fig. 4 (bottom panel). For comparison, we also show N_m vs t for the films on a homogeneous substrate.

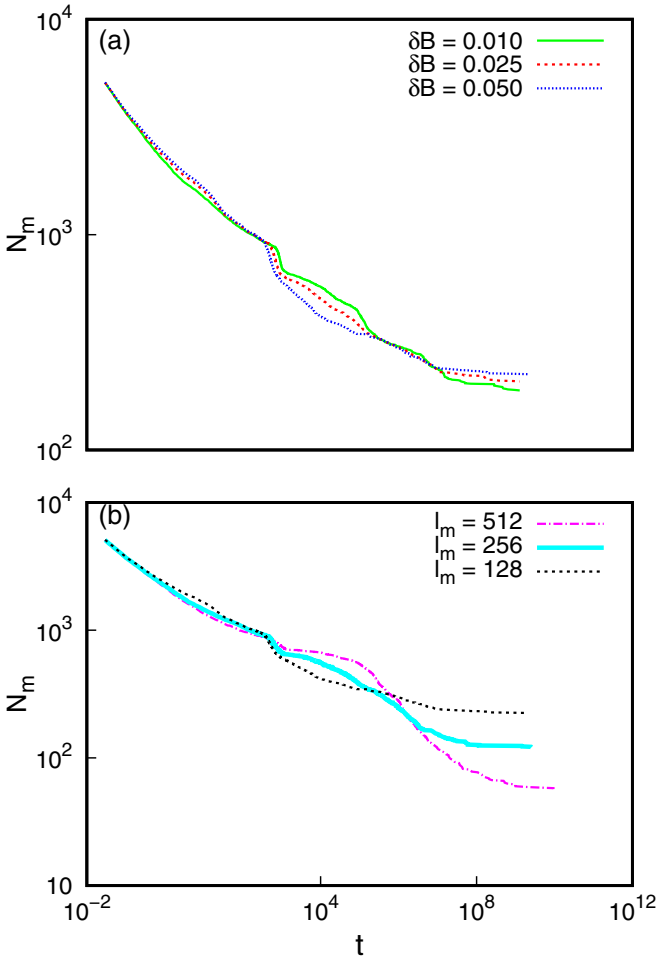

FIG. 6. Variation of number density of local maxima in $D = 2$ for (a) different strengths of disorder and (b) different patch sizes. The film thickness is 400 nm and $G = 0.105$. The system size is $8192L_M$, and the simulation parameters are (a) $B_m = -0.1$, $l_m = 256$, $\delta l = 32$ and (b) $B_m = -0.1$, $\delta B = 0.01$, $\delta l = 8$.

panel) for systems with and without disorder. The sudden drop in the total free energy for the 400-nm film is due to the simultaneous appearance of the two equilibrium phases. Before this time, the F values are comparable for both cases. The system without disorder proceeds slowly with logarithmic coarsening of domains. However, for the 400-nm film with disorder, F becomes constant with time, indicating that the system has reached a metastable state.

For the 172-nm film in Fig. 7(b), there is no significant difference between the cases with and without disorder on the timescales of our simulations. As we have emphasized earlier, defects do not undergo trapping by disorder sites. It is evident that the coarsening of domains (until they reach the equilibrium thickness) has a greater effect on lowering the free energy than arrest by the disorder.

B. Case with $D = 3$

The same methodology for introducing disorder has also been applied for $D = 3$ simulations. However, both sides of a patch are taken as independent random variables, i.e., each patch is rectangular (see Fig. 1). Figures 8 and 9 show the morphological evolution during true MPS of 400-nm (direct pathway) and 172-nm (defect pathway) films, respectively. The left-hand panels show the $D = 3$ snapshots, and the right-hand panels present the top view. Both the size and strength of the patches are random. (The parameters are provided in the figure caption.) Hence, some patches are more wettable than others. The chemical potential of the more wettable patches is lower. The droplets first appear on these and may also assume their shapes.

The 400-nm film undergoes true MPS through the direct pathway. Hence, both the equilibrium phases appear almost simultaneously. Then, coarsening becomes very slow, as evident from Figs. 8(e)–8(f). This phenomenon can be understood by recalling that each patch has its own free energy and chemical potential. Droplets are formed on more wettable patches. If these are surrounded by less wettable patches, further coarsening would mean an increase in the excess free energy of the system. As long as the decrease in interface leads to lowering of total free energy, coarsening will occur, but not thereafter. This leads to the pinning of the domains by the disorder. Thus, incoherent and odd-shaped structures

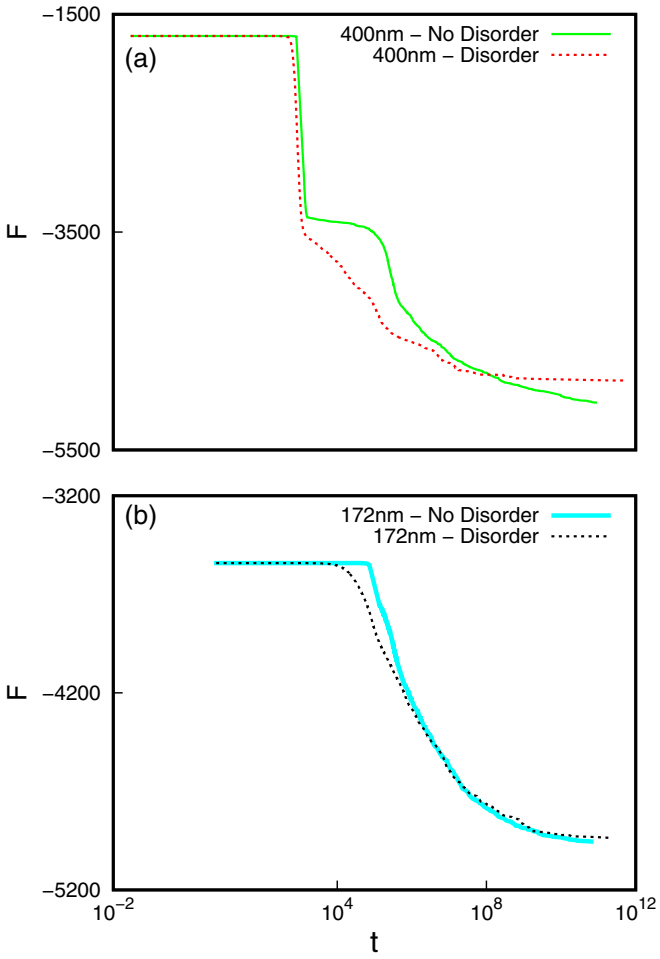

FIG. 7. Variation of free energy with time for the 400-nm film in Fig. 3 (top panel) and the 172-nm film in Fig. 4 (bottom panel). For comparison, we also show the free energy for the films on a homogeneous substrate.

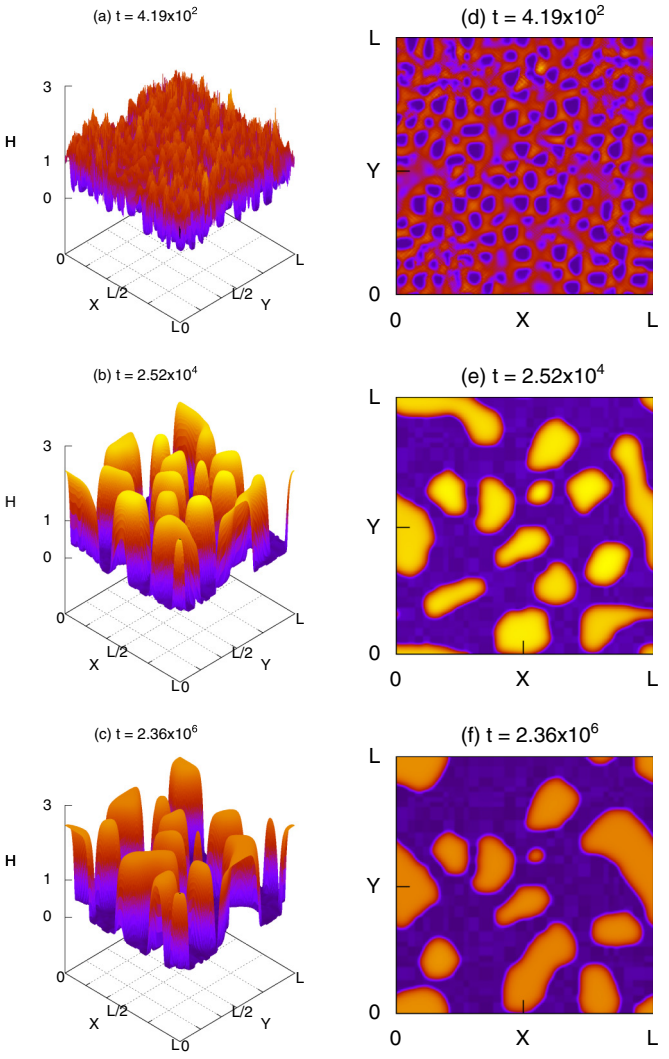

FIG. 8. Pattern formation during true MPS of a 400-nm film on a disordered substrate in $D = 3$. The frames (a)–(c) show the lateral view, and frames (d)–(f) show the top view. The system size is $(16L_M)^2$. The simulation parameters are $B_m = -0.1$, $\delta B = 0.05$, $l_m = 16$, $\delta l = 4$, and $G = 0.105$.

are formed which do not closely resemble the patterns of true MPS in thin film systems without disorder.

The 172-nm film shown in Fig. 9 undergoes true MPS through the defect pathway. Regardless of disorder, the coarsening of domains continues until the droplets reach the thickness corresponding to the thicker equilibrium phase. In the process, they overcome the disorder and retain their identity as individual droplets, instead of becoming incoherent structures.

As before, the minimization of free energy plays an important role in the self-organization of this thin-film system. Figure 10 shows the variation of F versus t (top panel) and entropy S versus t (bottom panel) for the 400- and 172-nm films. The configurational entropy is defined as a functional of the height field:

$$S\{H\} = -\int d\vec{X} H(\vec{X}, t) \ln H(\vec{X}, t). \tag{13}$$

For the 400-nm film, F and S become constant during the late stages, showing that the coarsening has been arrested. For the 172-nm film, F and S continue to decrease over our simulation time window, showing that the coarsening defects have overcome the pinning effects of the disorder.

Next, we discuss some statistical measures to characterize domain growth morphologies. A widely used statistical measure for probing the morphology is the *correlation function* [1]:

$$\begin{aligned} C(\vec{r}, t) &= \langle H(\vec{R}, t) H(\vec{R} + \vec{r}, t) \rangle - \langle H(\vec{R}, t) \rangle \langle H(\vec{R} + \vec{r}, t) \rangle \\ &= \langle \delta H(\vec{R}, t) \delta H(\vec{R} + \vec{r}, t) \rangle, \end{aligned} \tag{14}$$

where the angular brackets denote an averaging over independent runs with distinct initial conditions and disorder configurations. An equivalent measure, which is experimentally more relevant, is the *structure factor*, which is the Fourier transform of $C(\vec{r}, t)$ [1]:

$$S(\vec{k}, t) = \langle \delta H(\vec{k}, t) \delta H(-\vec{k}, t) \rangle = \int d\vec{r}\, e^{i\vec{k}.\vec{r}}\, C(\vec{r}, t). \tag{15}$$

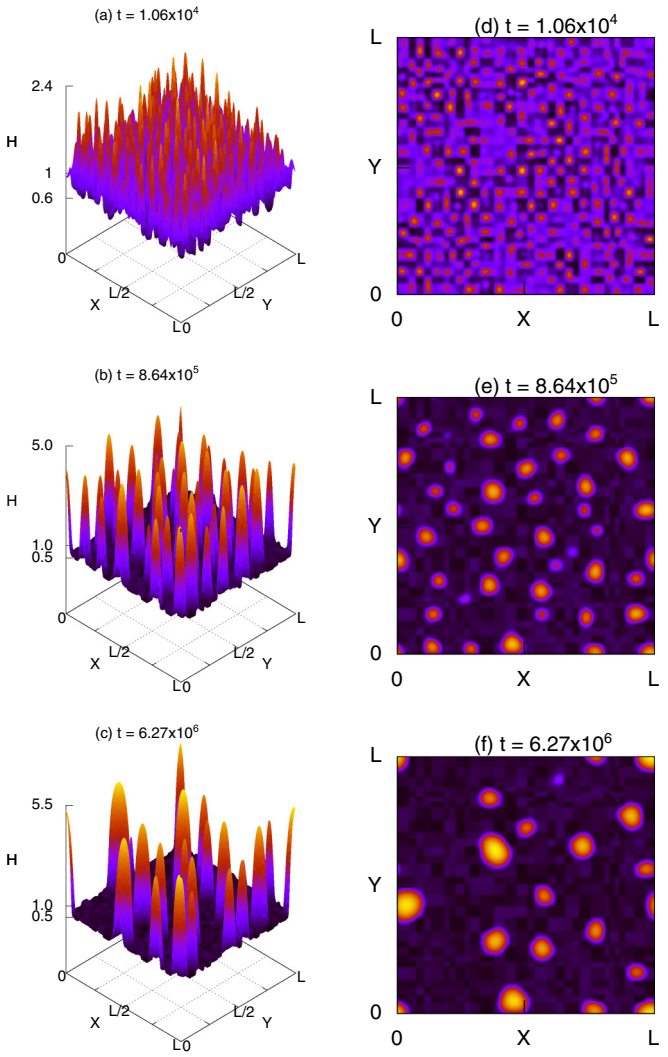

FIG. 9. Pattern formation during true MPS of a 172-nm film on a disordered substrate in $D = 3$. The frames (a)–(c) show the lateral view of the system, and frames (d)–(f) show the top view. The system size is $(16L_M)^2$. The simulation parameters are $B_m = -0.1$, $\delta B = 0.05$, $l_m = 16$, $\delta l = 4$, and $G = 3.5 \times 10^{-3}$.

Note that the structure factor is measured directly in scattering experiments, e.g., neutrons, light, x rays, etc.

In the late stages of evolution, when the initial fluctuations have been relaxed, there is only one time-dependent length scale $L(t)$ in the emerging pattern. The domain morphology is independent of time when scaled by $L(t)$; i.e., the system shows *dynamical scaling*. In that case, $C(\vec{r}, t)$ and $S(\vec{k}, t)$ have the scaling forms [1]

$$C(\vec{r}, t) = C(r, t) = f\left(\frac{r}{L}\right),$$
$$S(\vec{k}, t) = S(k, t) = L^d g(kL). \tag{16}$$

Here, we have assumed that the patterns are isotropic, and d denotes the substrate dimensionality.

Now we calculate the characteristic length scale $L(t)$. There are several methods of defining this quantity, but they are all equivalent (up to prefactors) in the scaling regime. In Sec. III A, we used the inverse defect density to define the length scale. Here, we obtain $L(t)$ as the inverse of the first moment of $S(k, t)$:

$$L = \langle k \rangle^{-1}, \tag{17}$$

where

$$\langle k \rangle = \frac{\int_0^\infty k S(k, t) dk}{\int_0^\infty S(k, t) dk}. \tag{18}$$

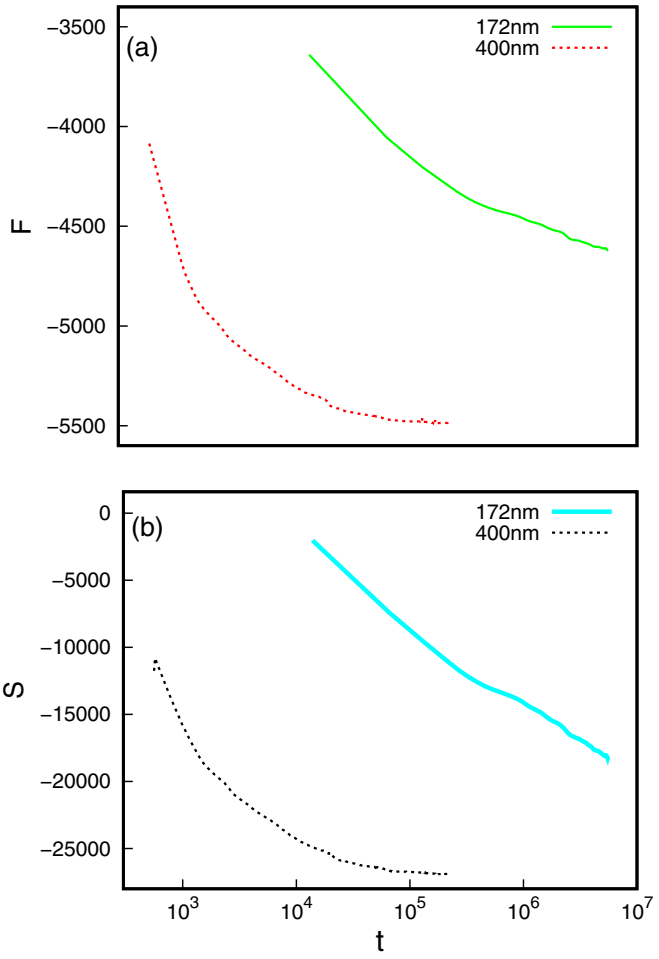

FIG. 10. (a) Variation of free energy during true MPS of $D = 3$ films for the pattern dynamics shown in Figs. 8 and 9. (b) Analogous to panel (a), but for the entropy.

In Fig. 11, we demonstrate the dynamical scaling of the structure factor by superposing data for $S(k, t)L^{-2}$ versus kL from three different times. In Fig. 11(a), we plot data for the 400-nm film, whose evolution is shown in Fig. 8. In this case, the structure factor data hardly changes as the evolution is approximately frozen over these timescales due to the trapping of interfaces by disorder sites. The structure factor tail is consistent with the Porod law, $S(k, t) \sim k^{-D}$, which characterizes scattering from sharp interfaces [1]. In Fig. 11(b), we plot data for the 172-nm film, whose evolution is shown in Fig. 9. This film is undergoing true MPS via the defect pathway. The defects are not trapped by the disorder sites, and pattern dynamics is unaffected over the timescales of our simulation. At early times, the structure factor does not show a clear Porod tail as the defects consist of

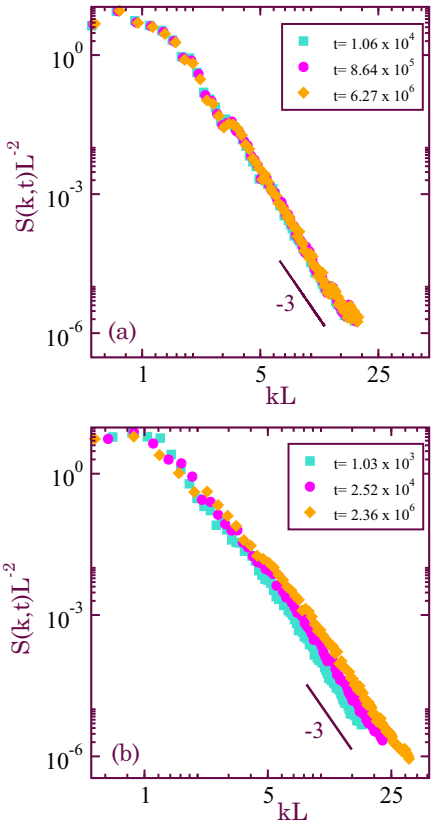

FIG. 11. Scaling plot of structure factors for the evolution shown in (a) Fig. 8 and (b) Fig. 9. The length scale L is obtained as the inverse of the first moment of the structure factor. The line of slope -3 denotes the Porod law, $S(k,t) \sim k^{-D}$, which is characteristic of scattering from sharp interfaces.

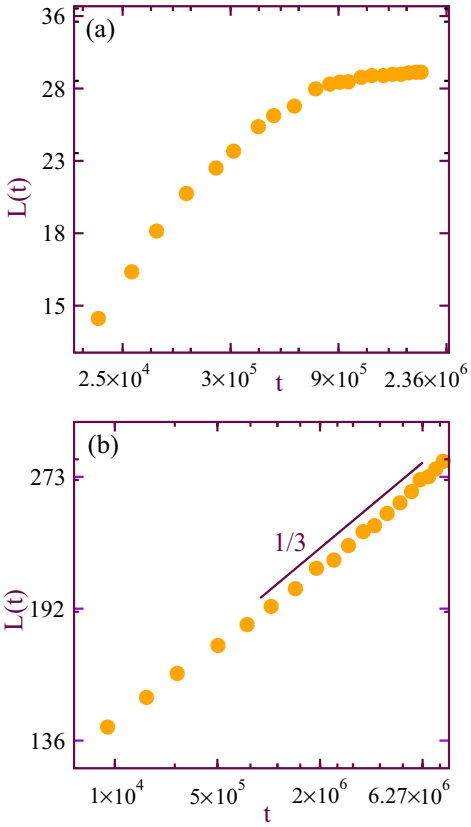

FIG. 12. Variation of length scale for the evolution shown in (a) Fig. 8 and (b) Fig. 9. The line of slope 1/3 denotes the Lifshitz-Slyozov growth law, $L(t) \sim t^{1/3}$.

ever-steepening walls. At late times, the system begins to establish stable interfaces (see Fig. 9). Thus, the Porod tail is recovered in the asymptotic regime.

In Fig. 12, we present data for $L(t)$ versus t on a log-log plot. In Fig. 12(a), we show data for the direct pathway followed by the 400-nm film. The length scale grows for a while and then saturates due to trapping of the domain walls. The data in Fig. 12(b) correspond to the defect pathway taken by the 172-nm film. In this case, there is no trapping due to disorder and defects coarsen via the LS growth law, $L(t) \sim t^{1/3}$, over the timescale of our simulation. In Fig. 12(b), we expect disorder effects to manifest themselves only subsequent to the formation of genuine domain walls between coexisting equilibrium phases.

IV. SUMMARY AND DISCUSSION

Let us conclude this paper with a summary and discussion of our results. We have studied the usual kinetic model of dewetting in liquid films on a coated substrate. The relevant free energy contains the standard substrate-film and coating-film interaction terms in conjunction with a gravity term, which is important in experimental situations. We also consider a disordered substrate, which is comprised of random-sized patches with inhomogeneous values of the wettability, i.e., the ratio of Hamaker constants of the substrate and coating.

In the absence of gravity, our earlier studies [28] have shown that the film undergoes morphological phase separation (MPS). In MPS, the film segregates into a thin equilibrium phase and droplets whose thickness continues to grow. This may be understood as a consequence of the fact that the Maxwell double-tangent construction locates the second equilibrium phase at height $H = \infty$. The presence of gravity dramatically changes this scenario and results in the existence of two equilibrium phases – a thin phase at H_1 and a thick phase at H_2. In the case with gravity, coarsening is driven by the desire of the system to reduce interfacial area between the coexisting equilibrium phases. We refer to this as true MPS, in contrast to MPS which is driven by defects between a thin phase and an ever-steepening droplet phase.

In this paper, we study how true MPS is affected by the presence of quenched disorder, which is experimentally inevitable. Our numerical studies uncover two scenarios for true MPS. This can be understood in the context of the free energy density, which is highly asymmetric (see Fig. 2).

(1) First, consider the case where the initial film thickness $H_0 = 1$ lies approximately midway between the equilibrium phase H_1 and H_2 [Fig. 2(a)]. The initial fluctuations are amplified exponentially and saturated to form H_1 and H_2 approximately simultaneously. We refer to this as the direct pathway. In the direct pathway, domain growth is driven

by genuine domain boundaries which are prone to trapping by disorder sites. In this case, the initial power-law domain growth crosses over to a much slower growth. In the absence of noise, the system freezes into a metastable state. In the presence of noise, we expect logarithmically slow coarsening at late times [29,30].

(2) Second, consider the case when $H_0 = 1$ is much closer to H_1 than H_2 [Fig. 2(b)]. In this case, the exponential growth of initial fluctuations is rapidly saturated to H_1 for $H < H_0$ but continues to grow for $H > H_0$. In this regime, we observe defect-driven coarsening similar to that in MPS. We refer to this scenario as the defect pathway. The defects are continuously steepening and are not prone to trapping by disorder sites. Therefore, there can be a prolonged regime of Lifshitz-Slyozov (LS) growth ($L \sim t^{1/3}$), which is not affected by disorder. The effects of disorder are only seen once equilibrium interfaces are formed. This onset could be extremely delayed for a highly asymmetric free energy.

For experimentalists, our study provides the range of initial film thicknesses which can overcome the trapping effects of disorder. Since the same equilibrium height can be achieved for various initial film thicknesses (note that the equilibrium heights depend on wettability B and coating thickness δ), our study enables us to pre-determine those film thicknesses which actually show the disorder effects and those which are unaffected by the disorder on a given timescale.

The above discussion is not specific to thin films under gravity. Clearly, it is applicable whenever the free-energy density is strongly asymmetric and admits two genuine phases via the Maxwell double-tangent construction. There are several experimental routes whereby this could be realized. We hope the numerical study presented here will motivate further interest in these problems. It would be particularly welcome if the proposed scenarios could be subjected to experimental verification.

ACKNOWLEDGMENT

S.P. is grateful to the Department of Science and Technology, India, for funding through a J. C. Bose fellowship.

APPENDIX: DERIVATION OF THIN-FILM EQUATION FROM THE NAVIER-STOKES EQUATION IN THE LUBRICATION APPROXIMATION

To derive the dynamical equation for thin liquid films, we consider a $D = 3$ Newtonian liquid film on a solid substrate in the (x, y) plane. The local film thickness $h(x, y, \tau)$ is along the z direction and is a function of time τ. We assume that the volume of the film is conserved, i.e., there is no loss due to evaporation. Following Ruckenstein and Jain [3], we derive the thin-film equation in the long-wavelength (or lubrication) approximation in which $h \ll L$, where L is the lateral size of the film. The Navier-Stokes (NS) equation for a viscous liquid with body forces $-\vec{\nabla}\phi$ is

$$\rho\left[\frac{\partial \vec{v}}{\partial \tau} + (\vec{v}\cdot\vec{\nabla})\vec{v}\right] = -\vec{\nabla}p - \vec{\nabla}\phi + \eta\nabla^2\vec{v}. \tag{A1}$$

Here, $\vec{v} \equiv (u, v, w)$ is the velocity at a fixed point in space and p is the pressure field. The quantities ρ and η are the density and viscosity, respectively. The x component of the NS equation is

$$u_\tau + uu_x + vu_y + wu_z = -\frac{P_x}{\rho} + \frac{\eta}{\rho}(u_{xx} + u_{yy} + u_{zz}),$$
$$P \equiv p + \phi. \tag{A2}$$

Let the typical scale of u be u_0. The typical length scale along the x, y axes is L, and along the z axis it is h. Therefore, we rescale variables as

$$x = Lx', \quad y = Ly', \quad z = hz', \quad u = u_0u', \quad v = u_0v',$$
$$w = u_0\frac{h}{L}w', \quad \tau = \tau_0\tau', \quad P = P_0P', \tag{A3}$$

where τ_0 and P_0 are the typical scales of time and P. In terms of the rescaled variables, Eq. (A2) becomes (assuming that h is a slowly varying function)

$$\frac{u_0}{\tau_0}u'_{\tau'} + \frac{u_0^2}{L}(u'u'_{x'} + v'u'_{y'} + w'u'_{z'})$$
$$= -\frac{P_0}{\rho L}P'_{x'} + \frac{\eta u_0}{\rho h^2}\left(\frac{h^2}{L^2}u'_{x'x'} + \frac{h^2}{L^2}u'_{y'y'} + u'_{z'z'}\right). \tag{A4}$$

Dividing both sides by $\eta u_0\rho/h^2$, we have

$$\frac{h^2}{\eta\rho\tau_0}u'_{\tau'} + \frac{u_0h}{\eta\rho}\cdot\frac{h}{L}(u'u'_{x'} + v'u'_{y'} + w'u'_{z'})$$
$$= -\frac{P_0h^2}{\rho^2\eta u_0L}P'_{x'} + \frac{1}{\rho^2}\left(\frac{h^2}{L^2}u'_{x'x'} + \frac{h^2}{L^2}u'_{y'y'} + u'_{z'z'}\right). \tag{A5}$$

Further, we assume that $(u_0h)/(\eta\rho) = O(1)$ and $h^2/(\eta\rho\tau_0) \ll 1$. Now, applying the lubrication approximation (i.e., $h/L \ll 1$) and keeping only dominant terms, we obtain

$$0 = -\frac{P_0h^2}{\eta u_0L}P'_{x'} + u'_{z'z'}. \tag{A6}$$

In terms of our original variables, Eq. (A6) becomes

$$P_x = \eta u_{zz} \tag{A7}$$

Similarly, $P_y = \eta v_{zz}$ and $P_z = 0$. Therefore, in the lubrication approximation, we have

$$P_x = \eta u_{zz}, \tag{A8}$$

$$P_y = \eta v_{zz}, \tag{A9}$$

$$P_z = 0. \tag{A10}$$

Further, for incompressible liquids we have

$$\vec{\nabla}\cdot\vec{v} = u_x + v_y + w_z = 0. \tag{A11}$$

Let us next consider the boundary conditions for the liquid film at the substrate ($z = 0$) and liquid-gas boundary ($z = h$). The *no-slip boundary condition* at the substrate implies that

$$u = v = w = 0, \quad \text{at } z = 0. \tag{A12}$$

The *zero-shear boundary condition* at the liquid-gas boundary implies that

$$u_z = v_z = 0, \quad \text{at } z = h. \tag{A13}$$

The condition of *pressure jump* at the liquid-gas boundary is

$$p - P = \gamma(h_{xx} + h_{yy}), \quad \text{at } z = h, \tag{A14}$$

where γ is the surface tension of the liquid film.

The *kinematic condition* for the equation of motion now becomes

$$h_\tau + uh_x + vh_y = w. \tag{A15}$$

We can obtain the velocity component u from Eq. (A8) after two integrations as

$$\eta u = P_x \frac{z^2}{2} + c'z + c'', \tag{A16}$$

where P_x is assumed to be independent of z. The boundary conditions at $z = 0$ and $z = h$ yield the values of c' and c''. The condition $u = 0$ at $z = 0$ yields $c'' = 0$. The condition $u_z = 0$ at $z = h$ yields $c' = -P_x h$. Therefore,

$$\eta u = P_x z\left(\frac{z}{2} - h\right). \tag{A17}$$

Similarly,

$$\eta v = P_y z\left(\frac{z}{2} - h\right). \tag{A18}$$

The component w is calculated from the incompressibility condition in Eq. (A11). Using Eqs. (A17) and (A18) for u, v, we have

$$\eta w = \frac{z^3}{6}(P_{xx} + P_{yy}) + \frac{z^2}{2}[(P_x h)_x + (P_y h)_y] + c''', \tag{A19}$$

where c''' is a constant of integration. The condition $w = 0$ at $z = 0$ gives $c''' = 0$. Therefore,

$$\eta w = \frac{z^3}{6}(P_{xx} + P_{yy}) + \frac{z^2}{2}[(P_x h)_x + (P_y h)_y]. \tag{A20}$$

Substituting u, v, w in Eq. (A15), we obtain

$$\eta h_\tau - zh(P_x h_x + P_y h_y) = -\tfrac{1}{6}z^3(P_{xx} + P_{yy}) + \tfrac{1}{2}z^2 h(P_{xx} + P_{yy}). \tag{A21}$$

At the liquid-gas interface ($z = h$), Eq. (A21) simplifies to

$$\eta h_\tau - h^2(P_x h_x + p_y h_y) = \tfrac{1}{3}h^3(P_{xx} + P_{yy}). \tag{A22}$$

Equation (A22) can be rewritten as

$$\frac{\partial h}{\partial \tau} = \frac{1}{3\eta}[(h^3 P_x)_x + (h^3 P_y)_y] = \vec{\nabla} \cdot \left[\frac{h^3}{3\eta}\vec{\nabla}P\right] \equiv \vec{\nabla} \cdot [M(h)\vec{\nabla}P]. \tag{A23}$$

Comparing Eq. (A23) with the continuity equation, we identify the current as $\vec{J} = -M(h)\vec{\nabla}P$, where the mobility $M(h) = h^3/(3\eta)$ is a function of the order parameter h. Now, from Eq. (A14) with $P = p + \phi$, we have at $z = h$:

$$P = p_0 + \phi - \gamma(h_{xx} + h_{yy}). \tag{A24}$$

Substituting P in Eq. (A23), we get

$$\frac{\partial h}{\partial \tau} = \vec{\nabla} \cdot \left[\frac{h^3}{3\eta}\vec{\nabla}(\phi - \gamma\nabla^2 h)\right]. \tag{A25}$$

Recall that $\phi = e'(h)$ is the derivative of the local free energy $e(h)$ resulting from the intermolecular forces and bulk forces. Equation (A25) describes the spatiotemporal evolution of an unstable thin liquid film and is known as the thin-film equation for liquids.

[1] S. Puri and V. K. Wadhawan (editors), *Kinetics of Phase Transitions* (CRC Press, Boca Raton, FL, 2009).

[2] R. C. Desai and R. Kapral, *Dynamics of Self-Organized and Self-Assembled Structures* (Cambridge University Press, Cambridge, UK, 2009).

[3] E. Ruckenstein and R. K. Jain, J. Chem. Soc., Faraday Trans. II **70**, 132 (1974).

[4] P. G. De Gennes, Rev. Mod. Phys. **57**, 827 (1985).

[5] A. Oron, S. H. Davis, and S. G. Bankoff, Rev. Mod. Phys. **69**, 931 (1997).

[6] P. G. De Gennes, F. Brochard-Wyart, and D. Quere, *Capillarity and Wetting Phenomena: Drops, Bubbles, Pearls, Waves* (Springer-Verlag, New York, 2004).

[7] R. V. Craster and O. K. Matar, Rev. Mod. Phys. **81**, 1131 (2009).

[8] D. Bonn, J. Eggers, J. Indekeu, J. Meunier, and E. Rolley, Rev. Mod. Phys. **81**, 739 (2009).

[9] C. V. Thompson, Annu. Rev. Mater. Res. **42**, 399 (2012).

[10] R. Mukherjee and A. Sharma, Soft Matter **11**, 8717 (2015).

[11] A. Kumar, C. Narayanam, R. Khanna, and S. Puri, Phys. Rev. E **96**, 062804 (2017).

[12] C. Narayanam, A. Kumar, R. Khanna, and S. Puri, Langmuir **33**, 3341 (2017).

[13] R. Khanna, N. K. Agnihotri, M. Vashishtha, A. Sharma, P. K. Jaiswal, and S. Puri, Phys. Rev. E **82**, 011601 (2010).

[14] S. Puri, D. Chowdhury, and N. Parekh, J. Phys. A: Math. Gen. **24**, L1087 (1991).

[15] C. Narayanam, A. Kumar, S. Puri, and R. Khanna, J. Phys. Chem. C **123**, 13958 (2019).

[16] A. Kumar, C. Narayanam, R. Khanna, and S. Puri, Phys. Rev. E **100**, 062803 (2019).

[17] R. Xie, A. Karim, J. F. Douglas, C. C. Han, and R. A. Weiss, Phys. Rev. Lett. **81**, 1251 (1998).

[18] R. Konnur, K. Kargupta, and A. Sharma, Phys. Rev. Lett. **84**, 931 (2000).

[19] M. Vashishtha, P. K. Jaiswal, R. Khanna, S. Puri, and A. Sharma, Phys. Chem. Chem. Phys. **12**, 12964 (2010).

[20] S. Puri and N. Parekh, J. Phys. A: Math. Gen. **25**, 4127 (1992).

[21] S. Puri and N. Parekh, J. Phys. A: Math. Gen. **26**, 2777 (1993).

[22] R. Paul, S. Puri, and H. Rieger, Europhys. Lett. **68**, 881 (2004); Phys. Rev. E **71**, 061109 (2005).

[23] M. Kumar, V. Banerjee, and S. Puri, Europhys. Lett. **117**, 10012 (2017).

[24] J. W. Cahn and J. E. Hilliard, J. Chem. Phys. **28**, 258 (1958).
[25] J. W. Cahn and J. E. Hilliard, J. Chem. Phys. **31**, 688 (1959).
[26] J. N. Israelachvili, *Intermolecular and Surface Forces* (Academic Press, San Diego, CA, 2011).
[27] T. Nagai and K. Kawasaki, Physica A (Amsterdam, Neth.) **134**, 483 (1986).
[28] P. K. Jaiswal, M. Vashishtha, S. Puri, and R. Khanna, Phys. Chem. Chem. Phys. **13**, 13598 (2011).
[29] E. Lippiello, A. Mukherjee, S. Puri, and M. Zannetti, Europhys. Lett. **90**, 46006 (2010).
[30] F. Corberi, E. Lippiello, A. Mukherjee, S. Puri, and M. Zannetti, J. Stat. Mech. (2011) P03016.